Aeroacoustic Simulations of Ducted Axial Fan and Helicopter Engine Nozzle Flows

Alexej Pogorelov, Mehmet Onur Cetin, Seyed Mohsen Alavi Moghadam, Matthias Meinke, and Wolfgang Schröder

Abstract The flow and the acoustic field of an axial fan and a helicopter engine jet are computed by a hybrid fluid dynamics – computational aeroacoustics method. For the predictions of the flow field a high-fidelity, parallelized solver for compressible flow is used in the first step. In the second step, the acoustic field is determined by solving the acoustic perturbation equations. The axial fan is investigated at a Reynolds number of $Re = 9.36 \times 10^5$ for two tip-gap sizes, i.e., $s/D_o = 0.001$ and $s/D_o = 0.01$ at a fixed flow rate coefficient $\Phi = 0.195$. A comparison of the numerical results of the pressure spectrum and its directivity with measurements show a good agreement which confirms the correct identification of the sound sources and the accurate prediction of the acoustic duct propagation. Furthermore, the results show in agreement with the experimental data a higher broadband noise level for the larger tip-gap size. In the second application, jets from three different helicopter engine nozzles at a Reynolds number of $Re = 7.5 \times 10^5$ are investigated, showing an important dependence of the jet acoustic near field on the presence of the nozzle built-in components. The presence of the centerbody increases the OASPL compared to the clean nozzle, where the inclusion of struts reduces the OASPL compared to the centerbody nozzle owing to the increased turbulent mixing caused by the struts which lesses the length and time scales of the turbulent structures shed from the centerbody.

1 Introduction

The prediction and reduction of noise generated by turbulent flows has become one of the major tasks of todays aircraft development and is also one of the key goals in European aircraft policy. Compared to the year 2000 the perceived noise level of flying aircraft should to be reduced by 65 % until the year 2050. To comply with new noise level regulations, reliable, efficient and accurate aeroacoustic predictions are required, i.e., for low noise design of technical devices such as axial fans or helicopter engine nozzles.

A. Pogorelov (✉) • M. Onur Cetin • S. Mohsen Alavi Moghadam • M. Meinke • W. Schröder
Institute of Aerodynamics, RWTH Aachen University, Wüllnerstr. 5a, 52062 Aachen, Germany
e-mail: a.pogorelov@aia.rwth-aachen.de

W.E. Nagel et al. (eds.), *High Performance Computing in Science and Engineering '16*, DOI 10.1007/978-3-319-47066-5_30

Fan industry increasingly demands for quieter and more efficient axial fans in a wide range of applications. A systematic quiet fan design, however, requires prediction methods for the acoustic field and sufficient details of the flow field to understand the intricate flow mechanisms, e.g. in the tip-gap region of the fan blade. Since measurements of the flow field in the rotating fan environment are difficult to perform, time-accurate numerical simulations such as highly resolved large-eddy simulations (LES) have shown to successfully predict the main flow phenomena [22–24], especially those in the tip-gap region since these can be a significant source of aerodynamic losses and noise emission.

Appreciable progress has been achieved over the last 20 years in the decrease of jet noise by using various noise reduction techniques such as high bypass ratio and design variations on the nozzle casing. These techniques have primarily focused on increasing the turbulent mixing by altering the nozzle design. In modern engines, the bypass ratio has already reached the limiting value and any further increase will aggravate the engine performance. Flow control inside the nozzle by additional built-in components such as wedges vanes etc. is an alternative approach and increasingly used to suppress the noise in the jet near field [14, 20].

The overall reliability of an acoustic prediction is prominently restricted with the quality of the flow field solution. To accurately capture the essential part of the turbulent spatial and temporal scales generated in the flow field highly resolved LES calculations are a must. That is such aeroacoustic analyses of high Reynolds number flow with complex geometries included in the computational domain require advanced computing resources.

In this paper the acoustic fields of a ducted axial fan and a helicopter engine nozzle are predicted by a hybrid fluid-dynamics-acoustics method. In a first step, large-eddy simulations are performed to determine the acoustic sources. In a second step, the acoustic field on the near and far-field is determined by solving the acoustic perturbation equations (APE) [6] on a mesh. The acoustic results of the axial fan are compared to experimental data [27].

This paper is organized as follows. First, the numerical methods are presented in Sect. 2. Subsequently, the LES and aeroacoustic results of the axial fan and nozzle-jet simulations are discussed in Sects. 3 and 4. Computational features and scalability analysis are given in Sect. 5. Finally, some conclusions are outlined in Sect. 6.

2 Numerical Method

An LES model based on a finite volume method is used to simulate the compressible unsteady turbulent flow by solving the Navier-Stokes equations. For the LES an implicit grid filter is assumed and the monotone integrated LES (MILES) approach [2] is adopted, i.e., the dissipative part of the truncation error of the numerical method is assumed to mimic the dissipation of the non-resolved subgrid-scale stresses. This solution method has been validated and successfully used, e.g.,

in [1, 16]. The governing equations are spatially discretized by using the modified advection upstream splitting method (AUSM) [19]. The cell center gradients are computed using a second-order accurate least-squares reconstruction scheme [10], i.e., the overall spatial approximation is second-order accurate. For stability reasons, small cut-cells are treated using an interpolation and flux-redistribution method [25]. A second order 5-stage Runge-Kutta method is used for the temporal integration. A parallel grid generator is used to create a computational hierarchical Cartesian mesh featuring local refinement [18]. The interested reader is referred to [19] for the details of the numerical methods, i.e., the discretization and computation of the viscid and inviscid fluxes. To determine the sound propagation and to identify the dominant noise sources the acoustic perturbation equations (APE) are applied. Since a compressible flow problem is considered, the APE-4 system is used [6].

To accurately resolve the acoustic wave propagation described by the acoustic perturbation equations in the APE-4 formulation [15] a sixth-order finite difference scheme with the summation by parts property [13] is used for the spatial discretization and an alternating 5–6 stage low-dispersion and low-dissipation Runge-Kutta method for the temporal integration [11]. On the embedded boundaries between the inhomogeneous and the homogeneous acoustic domain an artificial damping zone has been implemented to suppress spurious sound generated by the acoustic-flow-domain transition [26]. A detailed description of the two-step method and the discretization of the Navier-Stokes equations and the acoustic perturbation equations is given in [7].

3 Effect of Tip-Gap Size on Fan Aeroacoustics

In this subsection, a rotating low Mach number axial fan is investigated. In the first subsection, it is discussed how the gap size between blade tip and the outer casing wall affects the flow field at different operating conditions. All computations are performed at a fixed Reynolds number based on the rotational velocity and the diameter of the outer casing wall $Re = \frac{\rho \pi D_o^2 n}{\eta} = 9.36 \times 10^5$ and a fixed Mach number $M = \frac{\pi D_o n}{a} = 0.136$. Afterwards, the acoustic field is analyzed at the flow rate coefficient $\Phi = \frac{4\dot{V}}{\pi^2 D_o^3 n} = 0.195$ for two tip-gap widths $s/D_o = 0.001$ and $s/D_o = 0.01$.

3.1 Effect of Tip-Gap Size on the Overall Flow Field

The axial fan investigated in this section is shown in Fig. 1. The fan has five twisted blades out of which only one has been resolved in both LES and CAA computations to reduce the computational costs. The diameter of the outer casing wall is $D_o = 300$ mm and the inner diameter of the hub is $D_i = 135$ mm. The rotational

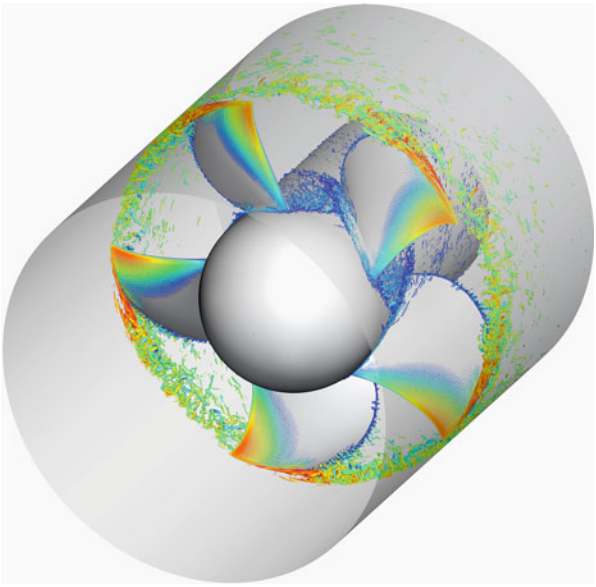

Fig. 1 Instantaneous contours of the Q-criterion inside the ducted axial fan configuration colored by the relative Mach number showing the vortical structures generated by the tip leakage flow at $\Phi = 0.195$ and $s/D_o = 0.005$

speed is $n = 3000$ rpm. As depicted in Fig. 1 for $\Phi = 0.195$ and $s/D_o = 0.005$, the existence of a gap between the blades tip and the outer casing wall and the pressure difference between the pressure and the suction side of the blades, lead to the development of a tip-gap vortex. Depending of the operating conditions the tip-gap vortex can be a major noise source in the axial fan, especially at low flow rate coefficients Φ, as demonstrated in [22] at $\Phi = 0.165$ and a tip-gap size of $s/D_o = 0.01$. At low flow rate coefficients the highly unsteady turbulent wake generated by the tip-gap vortex is shifted further upstream and impinges upon the leading edge of the neighboring blade. The intermittent interaction leads to a cyclic transition on the suction side of the blade. Acoustic measurements have shown broadband peaks in the specific sound power spectrum at frequencies corresponding to these phenomena. The decrease of the tip-gap width from $s/D_o = 0.01$ to $s/D_o = 0.005$ at $\Phi = 0.165$, stabilizes the tip-gap vortex and reduces the wandering motion of the turbulent wake such that the interaction with the leading edge of the neighboring blade and the cyclic transition triggered by this interaction vanish as discussed by Pogorelov et al. [23]. Instead, a permanent turbulent transition, which is triggered by a separation bubble at the leading edge was observed. The reduction of the tip-gap width leads to a strong decrease of the noise level. However, for the smaller tip-gap size, the turbulent wake still interacts with the pressure side of the blade. To separate the noise generated by the interaction and the phenomena triggered by this interaction from the self-generated noise of the tip-gap vortex

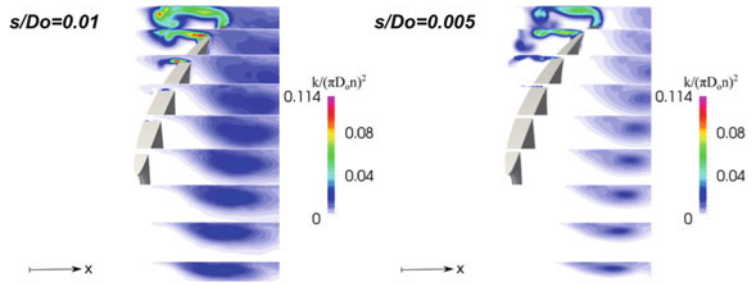

Fig. 2 Turbulent kinetic energy contours in several radial planes from $\theta = 30°$ to $\theta = 70°$, for $s/D_o = 0.01$ (*left*) and $s/D_o = 0.005$ (*right*)

it is important to analyze the acoustic field at higher flow rate coefficients and small tip-gap widths where no interaction with the neighboring blades is evident. Pogorelov et al. [24] analyzed the flow field at $\Phi = 0.195$ for the tip-gap widths $s/D_o = 0.005$ and $s/D_o = 0.01$. This study has demonstrated the strong impact of the tip-gap width on the size and shape of the tip-gap vortex. It has been shown, that due to the stronger curvature and the smaller diameter of the tip-gap vortex for $s/D_o = 0.005$, the entire turbulent wake passes the neighboring blade without any interaction, where for $s/D_o = 0.01$ several vortical structures of the turbulent wake reach the trailing edge of the blade at the pressure side, as depicted in Fig. 2. Therefore, for tip-gap sizes below $s/D_o = 0.005$ no interaction with the neighboring blades is expected. In the following subsection, the acoustic field of the flow field at $\Phi = 0.195$ for $s/D_o = 0.001$ and $s/D_o = 0.01$ is analyzed. For the source computation, required for the acoustic analysis LES have been conducted for both operating conditions. The computational mesh resolving one out of five blades has approx. 140 million grid points. Two full rotations have been required to obtain a fully developed flow field. Data from another two full rotations has been used for statistical analysis. In total, 1440 samples were recorded which required 8.6 TB of disc space. The CPU time was approx. 200 h and the computations were conducted on approx. 6000 CPUs.

3.2 Effect of Tip-Gap Size on the Acoustic Field

In the following, the acoustic field is numerically analyzed by a hybrid fluid-dynamics-aeroacoustics method. The acoustic field on the near field and far field is determined by solving the APE [6] in the rotating frame of reference on a mesh for a single blade consisting of approx. 1060×10^6 grid points which comprises a 72° segment of a rotating axial fan with periodic boundary conditions in the azimuthal direction. The computations are performed for two tip-gap sizes namely, $s/D_o = 0.001$ and $s/D_o = 0.01$ at the flow rate coefficient $\Phi = 0.195$. Based on the LES solution of the turbulent flow field, from which the acoustic sources are

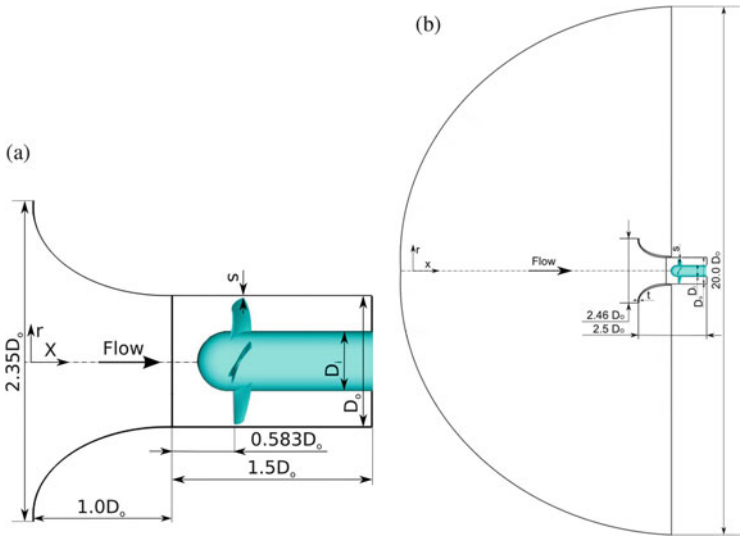

Fig. 3 (**a**) Schematic view of the LES and (**b**) the acoustic configuration of an axial fan

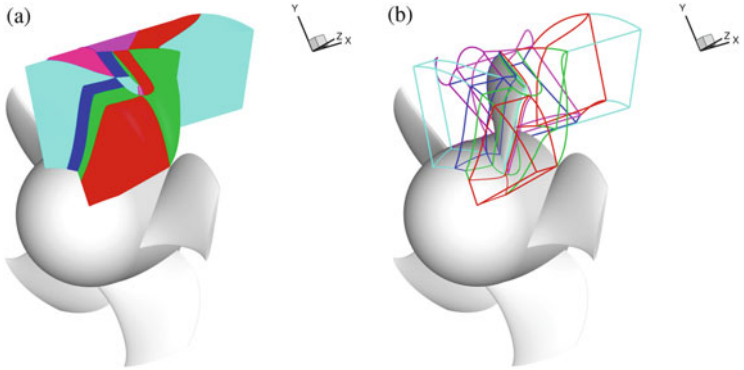

Fig. 4 The multi-block structured mesh in the acoustic source region resolving one out of five blades of the axial fan; (**a**) view of the overall mesh; (**b**) detailed topological view of the mesh

determined, the near far-field acoustics is computed by solving the APE-4 system. Since the contribution of entropy and non-linear terms can be neglected in this study, only the vortex sound sources are taken into account.

A schematic view of the present computational setup is shown in Fig. 3 In a first step, the turbulent flow fields are determined by LES for the two configurations for 24 full rotations. Subsequently, the source terms are computed in the source region which contains approximately 122 million grid points with the same mesh resolution as the corresponding LES mesh. Figure 4 shows the computational mesh used for computing the source terms. The instantaneous distribution of the dominant

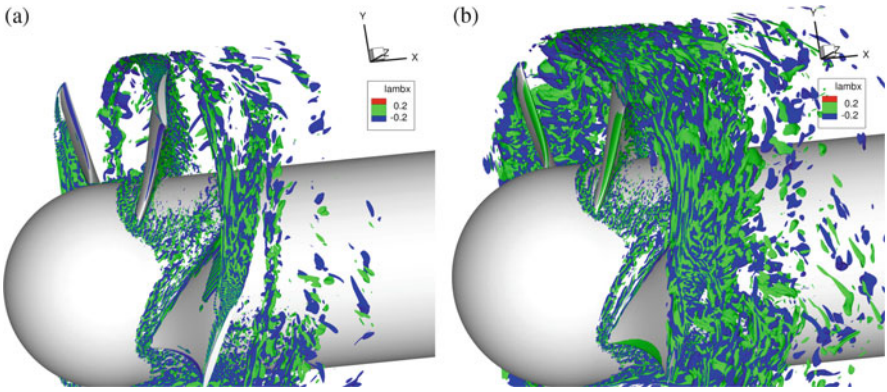

Fig. 5 Instantaneous contours of the Iso-surface of axial component of the fluctuating Lamb vector showing the major sound sources around the blade; (**a**) configuration $s/D_o = 0.001$; (**b**) configuration $s/D_o = 0.01$

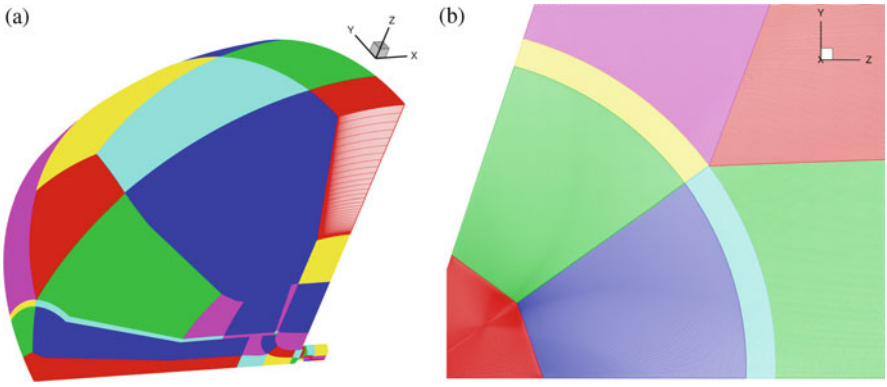

Fig. 6 The multi-block structured mesh for the acoustic domain resolving one out of five blades of the axial fan; (**a**) view of the overall mesh; (**b**) detailed view of the mesh at far-field

fan noise sources, which is the fluctuating Lamb vector $\mathbf{L}' = (\Omega \times \mathbf{u})'$, for the two configurations is shown in Fig. 5

It is clearly visible that the strongest sources occur in regions with the highest turbulent kinetic energy, i.e., in the tip vortex, blade wake and on the hub region. Moreover, the noise sources generated by the bigger tip-gap size $s/D_o = 0.01$ exhibits higher amplitudes compared to the smaller tip-gap size $s/D_o = 0.001$. In a second step, the acoustic field is predicted based on the corresponding LES results. The computational mesh used for the LES is extended in the axial and radial direction up to $20D_o$. The grid spacing around the microphones positions is $\Delta x_{mic}/D_o \approx 5 \times 10^{-3}$, so that for 10 points per wavelength, the maximum frequency resolvable by the grid is about 10 kHz. The acoustic mesh including some details of the mesh resolution in the far-field are shown in Fig. 6. The time step of the

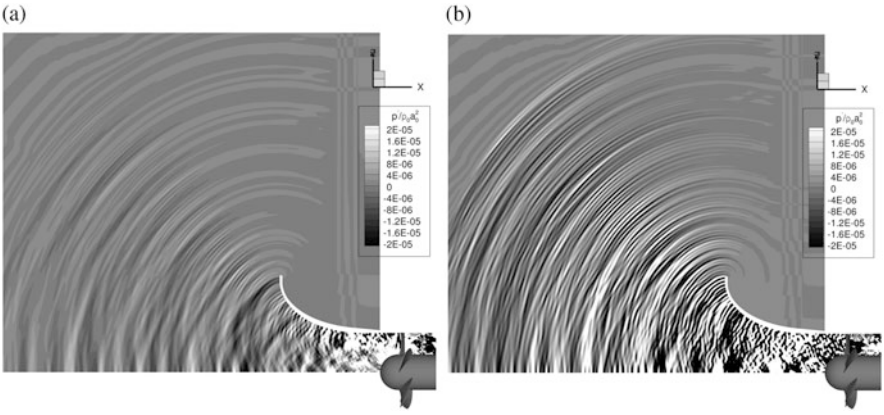

Fig. 7 Instantaneous contours of the fully developed acoustic field showing the acoustic duct propagation into the far-field; (**a**) configuration $s/D_o = 0.001$; (**b**) configuration $s/D_o = 0.01$

acoustic analysis is $\Delta t = 4.613 \times 10^{-3} D_o/a_\infty$ to ensure a fully stable numerical solution. Based on 1500 LES snapshots at a time interval of $\Delta t_{src} = 0.0224 D_o/a_\infty$, the source terms are computed and a least square optimized interpolation filter [9] using $N = 10$ source samples is used to provide source fields at every Runge-Kutta time-integration step. The acoustic computations are run for a non-dimensional time period of $39 D_o/a_\infty$. Explicit low-pass filtering at every 5th Runge-Kutta time-integration step is used to avoid numerical oscillations. Additionally, a sponge layer is used in order to damp acoustic wave reflections at far-field and downstream of the fan.

In Fig. 7 the acoustic fields generated by the turbulent structures of the rotating axial fan for the two configurations are illustrated. The acoustic pressure field shows noise generation at a higher frequency for the configuration $s/D_o = 0.01$ with the bigger tip-gap size and a noise generation at lower frequency for the configuration $s/D_o = 0.001$ with the smaller tip-gap size. In the following acoustic analysis, the computed sound pressure spectra at the circle C1 which is defined in Fig. 8, are compared with the experimental data [27]. For the comparison of the numerical results with experimental data, the acoustic signals are analyzed on circle C1 and circle C2, which are located 1.30 and 1.0 m from suction mouth of the fan. The acoustic measurements were carried out in the fixed frame of reference. In order to compare the computed sound spectra in rotating frame of reference with the experimental findings, 1001 probes are equally distributed on each circle of 72°. First, the position of the microphones are calculated in the fixed frame of reference and then sound pressure spectrum for all processed microphones are computed. Finally, the sound pressure spectrum of all microphones are averaged. The computed sound pressure spectra at the circle C1 and circle C2 are shown in Figs. 9 and 10 respectively.

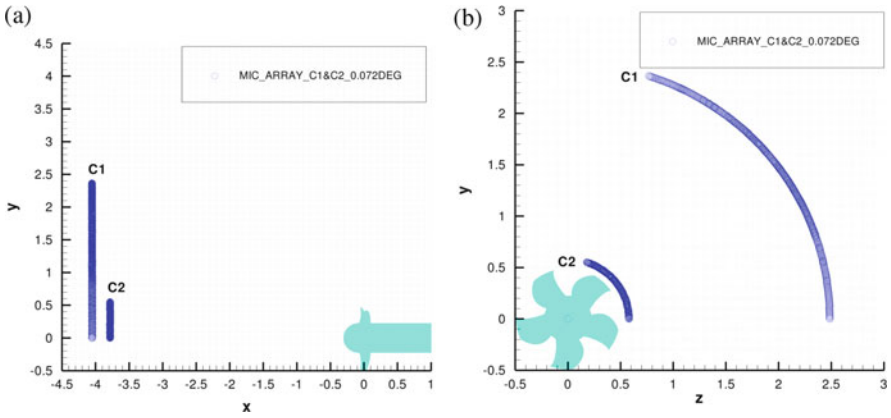

Fig. 8 Schematic of the virtual microphone positions for the two acoustic configurations; (**a**) side view; (**b**) front view

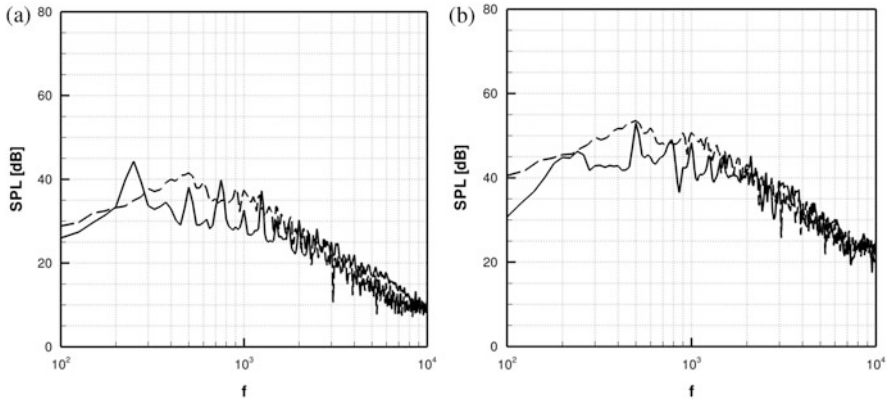

Fig. 9 Sound spectra at the far-field locations circle C1; (**a**) configuration $s/D_o = 0.001$; (**b**) configuration $s/D_o = 0.01$; comparison of the (−−) numerical results with the (—) experimental results [27]

The evaluation of the sound pressure level at the circle C1 and the circle C2 show a convincing agreement especially at the broadband noise level. However, considering the circle C2 towards center line of the axial fan, the computed sound pressure level at the lower frequencies deviate from the experimental measurements which is due to the fact that one blade acoustic simulations using periodic boundary condition lacks certain low wave number ranges which is clearly observable in corresponding spectral analysis. In addition, a higher noise level of the case with the bigger compared to the smaller tip-gag size is clearly reproduced by the numerical simulation method.

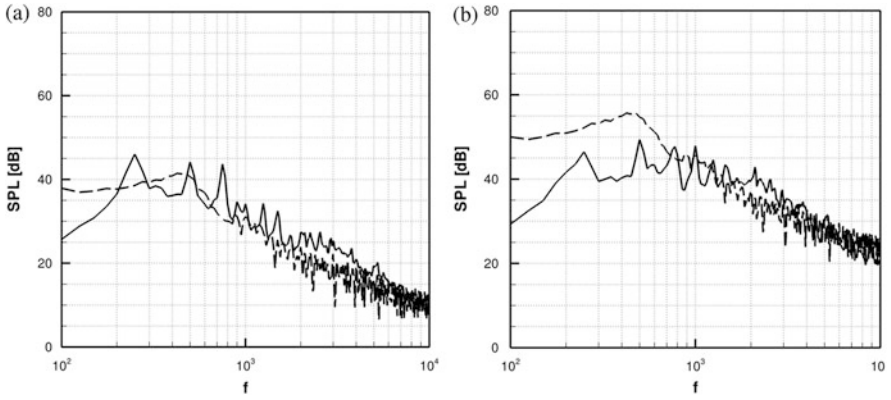

Fig. 10 Sound spectra at the far-field locations circle C2; (**a**) configuration $s/D_o = 0.001$; (**b**) configuration $s/D_o = 0.01$; comparison of the (−−) numerical results with the (—) experimental results [27]

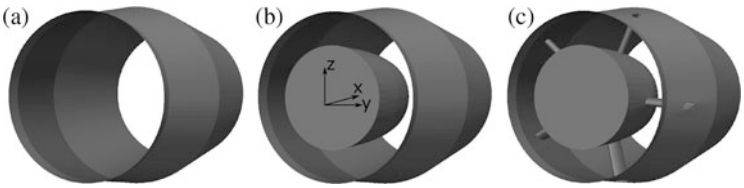

Fig. 11 Rear section of the nozzle geometry (**a**) clean nozzle hj_1, (**b**) centerbody nozzle hj_2, (**c**) centerbody-plus-strut nozzle hj_3

4 Effect of the Interior Nozzle Geometry on Jet Aeroacoustics

In this section, simulation results of round jets emanating from a three variants of non-generic nozzle are presented. First the flow field of the three nozzle configurations at a Reynolds number of $\mathrm{Re} = 7.5 \times 10^5$ and a Mach number of $\mathrm{M} = 0.341$ are conducted and thereafter, the acoustic field is computed whose acoustic source terms are determined by LES data.

4.1 Flow Field

The nozzle geometry corresponds to a divergent helicopter engine nozzle. Figure 11 shows the interior of three variants of the engine nozzle, the clean nozzle hj_1, the centerbody nozzle hj_2, and the centerbody-plus-strut nozzle hj_3 which are identical except for the centerbody and the struts which support the centerbody.

Table 1 Simulation features and mesh parameters of the flow and the acoustic field solutions

	Clean nozzle (hj_1)	Centerbody nozzle (hj_2)	Centerbody-plus-strut nozzle (hj_3)
	Flow field		
Mach number M_j	0.341	0.341	0.341
Reynolds number Re_{D_e}	750,000	750,000	750,000
Mesh points	335×10^6	329×10^6	328×10^6
Number of samples	2251	2251	2251
	Acoustic field		
Mesh points	108.5×10^6	108.5×10^6	108.5×10^6

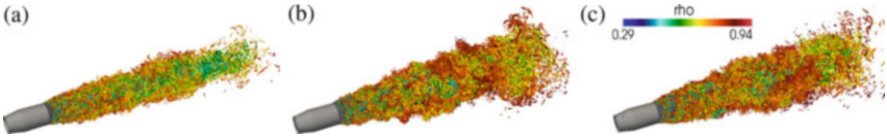

Fig. 12 Contours of the Q-criterion color coded by density for three geometries (**a**) hj_1, (**b**) hj_2, (**c**) hj_3

The operating conditions of the last turbine stage are set at the inlet boundary which were taken from the measurements of a full-scale turbo-shaft engine [21]. Isotropic synthetic turbulence is injected at the inlet plane with approx. 10 % turbulence intensity [17]. For the outflow and lateral boundaries of the jet domain, static pressure is kept constant and other variables are extrapolated from the internal domain. To damp the numerical reflections at the boundaries, sponge layers are prescribed [8]. At the nozzle-wall a no-slip condition with a zero pressure and density gradient is applied. Hierarchically refined Cartesian meshes are used for the flow field computations and a grid convergence study of the centerbody nozzle hj_2 configuration is studied in [4, 5]. The essential mesh and simulation parameters of the analysis of the flow and the acoustic fields are summarized in Table 1.

The overall turbulent structures in the jet are visualized in Fig. 12 by the contours of the instantaneous Q-field [12] for the three configurations. Since the same threshold value for the Q-contours is used, the various widening of the free jets can be deduced from this illustration. In other words, Q-fields evidence the smaller spreading of the jet exhausting from the clean nozzle hj_1.

The modified turbulence field influences the jet characteristics downstream of the nozzle exit. This is illustrated by the contours of the mean axial velocity in the free jet region in Fig. 13. The mean velocity on the centerline decreases much more strongly for the hj_2 and hj_3 geometries than for the clean nozzle which possesses a standard jet plume shape. Furthermore, the asymmetric velocity distribution caused by the struts is visible in the jet field just downstream of the exit. However, further downstream hardly any asymmetric influence of the struts is observed.

The mean axial velocity distribution normalized with the average nozzle exit axial velocity $u_{ne} = \frac{1}{A}\int \mathbf{u} \cdot \mathbf{n} dA$ on the centerline starting at the rear face of the

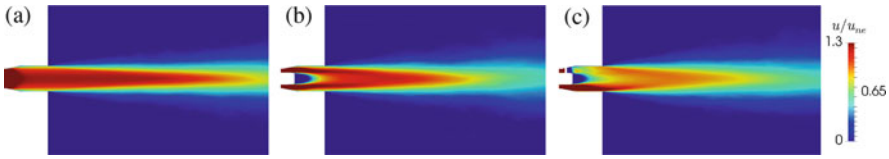

Fig. 13 Contours of the mean axial velocity in the free jet region for three geometries (**a**) hj_1, (**b**) hj_2, (**c**) hj_3

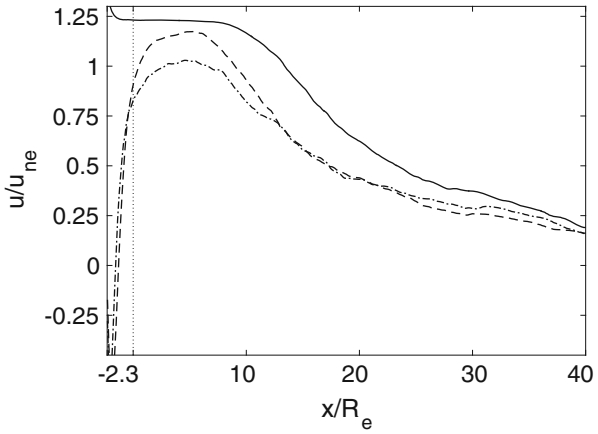

Fig. 14 Streamwise distribution of the axial velocity on the *centerline* $r/R_e = 0$ for (—) hj_1, (——) hj_2, (-·-) hj_3

centerbody $x/R_e = -2.3$ where $R_e = D_e/2$ is the nozzle exit radius, is presented in Fig. 14. Note that the decreasing distribution between $-2.3 < x/R_e < -1.1$ of the clean nozzle hj_1 is due to the divergence of the nozzle casing. Besides the impact of the diverging part of the nozzle, the velocity distribution on the centerline of the clean nozzle hj_1 undergoes the standard decay. Downstream of the exit of the nozzle the centerline velocity remains constant till the free-shear layers start to merge causing the decay of the centerline velocity. For the centerbody and the centerbody-plus-strut configurations hj_2 and hj_3 the distribution of the streamwise velocity on the centerline is characterized by the pronounced recirculation in the base region of the centerbody. Downstream of this reversal flow neither the hj_2 nor the hj_3 centerline velocity reach the value of the clean nozzle. To be more precise, the peak value of the centerline velocity of the hj_2 solution is diminished by 11 % and that of the hj_3 solution by 22 % compared to the hj_1 value. When the velocity decay sets in the hj_2 and hj_3 solutions approach the hj_1 distribution such that at $x/R_e \geq 35$ the centerline velocities almost agree.

Figure 15 shows the streamwise distribution of the axial and radial turbulence intensity on the centerline. The intensity of the axial velocity fluctuations in Fig. 15a rises rapidly downstream of the nozzle exit. At the nozzle exit the centerbody nozzle hj_2 and the centerbody-plus-strut nozzle hj_3 solutions possess much higher

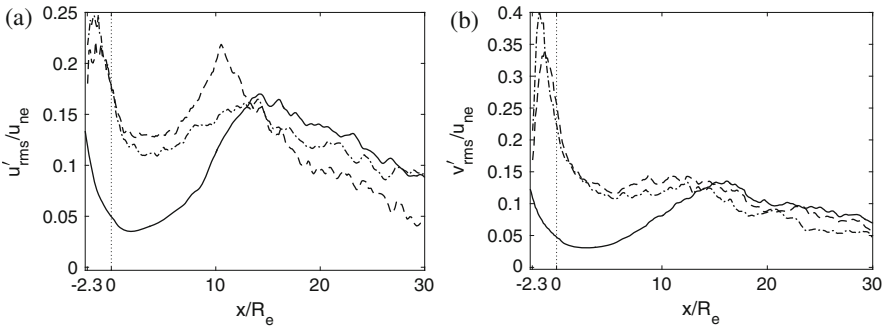

Fig. 15 Streamwise distribution at $r/R_e = 0$ of (**a**) the rms axial velocity and (**b**) the rms radial velocity for (—) hj_1, (——) hj_2, (-·-) hj_3

turbulence intensity than the clean nozzle hj_1 solution due to the enhanced turbulent mixing caused by the centerbody and the struts. Further downstream of $x/R_e \geq 15$ all profiles of the rms axial and radial velocities show a similar decaying trend.

4.2 Acoustic Field

The acoustic perturbation equations (APE) are applied to determine the sound propagation and to identify a dominant noise source excited by the hot jets. Since a compressible flow problem is tackled the APE-4 system is used [6].

For the computations a time step $\Delta t = 0.011 R_e/a_\infty$ is chosen to obtain stable numerical solutions. The acoustic analyses include the sound waves whose maximum wavenumber $k_{\max} = 2\pi/\lambda_{\min}$ is approximately $0.36\pi/R_e$. The source fields are provided for all Runge-Kutta steps using a least squares optimized interpolation algorithm [9]. The time interval reconstructed by the 2251 LES snapshots is $T_{\text{total}} = 148.5 R_e/u_e$.

The acoustic simulation setup and mesh details are discussed at length in [3].

In Fig. 16 the acoustic field determined by the aforementioned numerical schemes is illustrated. The contours of the acoustic pressure are ranged in $p' \leq 5 \times 10^{-6} \rho_0 a_0^2$ near the jet nozzle region. The acoustic pressure of the configuration hj_1 possesses smaller amplitudes than the other two configurations hj_2 and hj_3. At the nozzle exit in Fig. 13 the mean axial velocity in the radial direction ($r = \sqrt{y^2 + z^2}$) decreases for the clean nozzle configuration hj_1. The turbulent fluctuations in the shear layer are less pronounced for the single jet hj_1 as discussed in Fig. 15. These are the major reason of a low acoustic energy in the single jet hj_1.

The overall acoustic level in Fig. 17 evidences the low acoustic emission of the single jet hj_1. The profiles of three acoustic fields are obtained by the microphones aligned in the axial direction at the sideline location $8R_e$ away from the jet centerline. The dominant wave radiation occurs in the upstream position due to

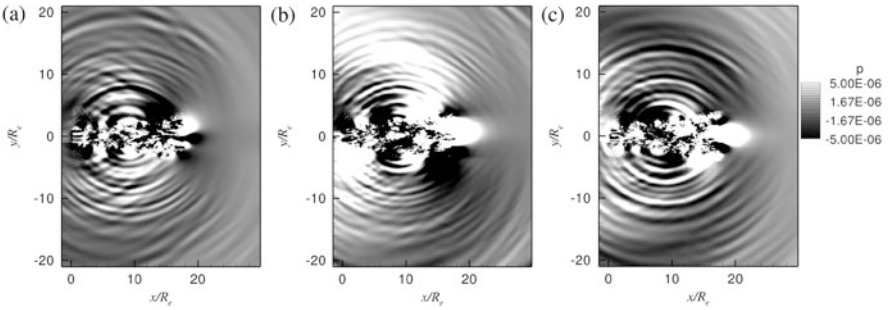

Fig. 16 Acoustic pressure contours in the range of $|p'/\rho_0 a_0^2| \leq 5 \times 10^{-6}$ on the $z = 0$ plane, (**a**) hj_1, (**b**) hj_2, and (**c**) hj_3

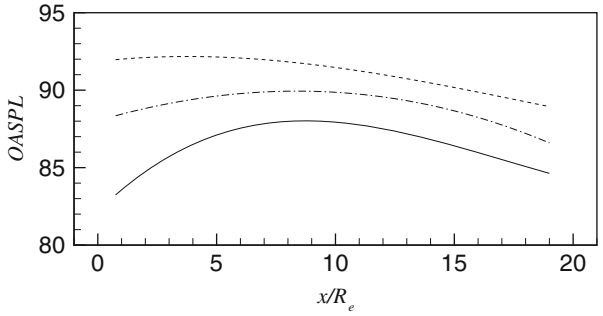

Fig. 17 Overall sound pressure level in dB at the radial distance of $8R_e$ from the jet centerline, (—) hj_1, (——) hj_2, (-··-) hj_3

the unperturbed jet core in the nozzle exit area. The microphone in a downstream location captures the acoustic waves at a relatively farther distance from the end of the jet core. The centerbody nozzle configuration hj_2 generates the most powerful acoustics which shows 3 dB larger OASPL at a streamwise position $x = 10R_e$ compared to the single jet hj_1. The additional turbulence mixing by struts in the configuration hj_3 reduces the acoustic generation by approximately 2–4 dB over the streamwise position $R_e \leq x \leq 19R_e$. The acoustic directivity of the single jet hj_1 shows a silent zone in the upstream position $x \leq 5R_e$. Compared with the findings of the single jet (hj_1) the axial profiles of the other jets (hj_2 and hj_3) show an approximately 2–9 dB higher acoustic pressure.

In Fig. 18 the acoustic spectra of a single and two centerbody jets are compared. The sound pressure is determined at the coordinates ($x = 3R_e$, $r = 8R_e$) for the sideline acoustics in Fig. 18a and ($x = 18R_e$, $r = R_e$) for the downstream acoustics in Fig. 18b. The sideline acoustics in Fig. 18a display a large increase of power spectral density in the frequency range $fD_e/u_e = 0.3 \sim 0.8$, where f is the frequency and u_e nozzle exit average velocity. The peaks are located at $fD_e/u_e = 0.45$ for the single jet hj_1 and at $fD_e/u_e = 0.5 \sim 0.6$ for the jets with a centerbody hj_2,

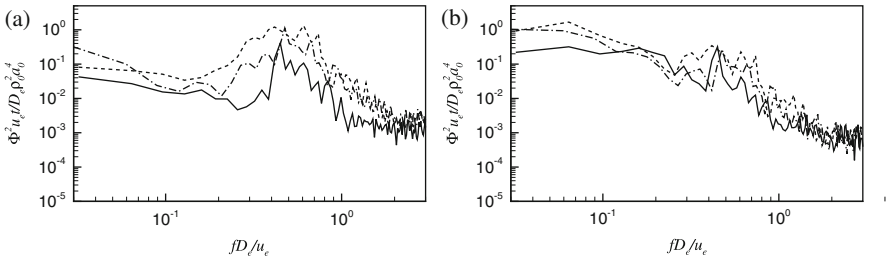

Fig. 18 Power spectra of the acoustic pressure signals determined at the coordinates (**a**) $x/R_e = 3,\ r/R_e = 8$ and (**b**) $x/R_e = 18,\ r/R_e = 8$: (—) hj_1, (−−) hj_2, (-·-) hj_3

hj_3. The downstream acoustics in Fig. 18b shows the pronounced low frequency radiation at $fD_e/u_e \leq 0.1$. The acoustic peaks occur at the same frequency range identified in the sideline acoustics. As indicated by the spectra of hj_2 and hj_3 the increase of the acoustic power becomes more prominent when the turbulent fluctuations increase. The sound generation of a hot jet includes two features. The first feature is the downstream acoustics due to the large scale turbulence in the shear layers and the second one is the sideline acoustics enhanced by the temperature gradient. Figure 18a illustrates the differences of the sideline acoustics. The acoustic radiation almost perpendicular to the jet axis is clearly intensified for the jets with a centerbody hj_2, hj_3 more than that of the single jet hj_1. Besides, in the frequency band $0.1 \leq fD_e/u_e \leq 0.5$ the acoustic level of the centerbody-plus-strut configuration hj_3 is reduced compared to that of the centerbody configuration hj_2.

5 Computational Specifications and Scalability Analysis

The simulations of the acoustic field were carried out on the CRAY XC40 at HLRS Stuttgart, containing two socket nodes with 12 cores at 2.5 GHz. Each node is equipped with 128 GB of RAM, i.e., each core has 5.33 GB of memory available for the computation. Strong scaling experiments were conducted to demonstrate the scalability of the APE-4 solver. Five core numbers were used, i.e., 512, 1024, 2048, 4096, and 8192. Furthermore, the results are based in 100 integrated time steps using a mono-block cubic grid with 256^3 grid points and periodic boundary conditions. The overall speedup as a function of the number of cores shown in Fig. 19 proves the good scalability of the code.

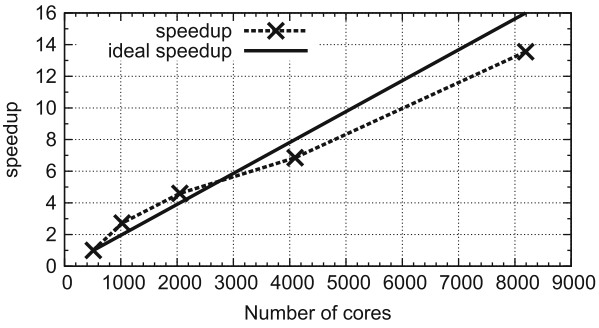

Fig. 19 Strong scaling experiment; Simulations were performed for 100 integrated time steps using five number of cores, i.e., 512, 1024, 2048, 4096 and 8192

6 Conclusion

The flow and the acoustic field of a ducted axial fan and a subsonic jet including the nozzle geometry were simulated by a hybrid CFD/CAA method. First, the flow field was computed by an LES and subsequently, the acoustic field was determined by solving the APE.

For the axial fan, two configurations with different tip-gap sizes, i.e. ,$s/D_o = 0.001$ and $s/D_o = 0.01$ at the flow rate coefficient $\Phi = 0.195$ were performed and the results were compared to reference data. The findings showed that the diameter and strength of the tip vortex increase with the tip-gap size, while simultaneously the efficiency of the fan decreases. Increasingly the tip-gap size led to the strongest sound sources occur in the tip-gap regions as well as at wake of the fan blade. In the second step, acoustic field was determined by solving APE-4 system in rotating frame of reference. The overall agreement of the pressure spectrum and its directivity with measurements confirm the correct identification of the sound sources and accurate prediction of the acoustic duct propagation. The results show that the larger the tip-gap size the higher the broadband noise level.

Next, three turbulent jets emanating from of a clean divergent annular reference nozzle, a configuration with a centerbody and a geometry with a centerbody plus 5 equidistantly distributed struts were considered. The results showed an important dependence of the jet acoustic near field on the presence of the nozzle built-in components. For example, on the one hand, the presence of the centerbody increased the OASPL up to 6 dB compared to the clean nozzle, on the other hand, inclusion of the 5 struts reduced the OASPL up to 4 dB compared to the centerbody nozzle owing to the increased turbulent mixing caused by the struts which lessen the length and time scales of the turbulent structures shed from the centerbody.

Acknowledgements The research has received funding by the German Federal Ministry of Economics and Technology via the “Arbeitsgemainschaft industrieller Forschungsvereinigungen Otto von Guericke e.V.” (AiF) and the “Forschungsvereinigung Luft- und Trocknungstechnik e.V.”

(FLT) under the grant no. 17747N (L238) as well as from the European Community's Seventh Framework Programme (FP7, 2007–2013), PEOPLE program under the grant agreement No. FP7-290042 (COPAGT project). Computing resources were provided by the High Performance Computing Center Stuttgart (HLRS) and by the Jülich Supercomputing Center (JSC).

References

1. Alkishriwi, N., Meinke, M., Schröder, W.: Large-eddy simulation of streamwise-rotating turbulent channel flow. Comput. Fluids **37**, 786–792 (2008)
2. Boris, J.P., Grinstein, F.F., Oran, E.S., Kolbe, R.L.: New insights into large eddy simulation. Fluid Dyn. Res. **10**, 199–228 (1992)
3. Cetin, M.O., Koh, S.R., Meinke, M., Schröder, W.: Numerical analysis of the impact of the interior nozzle geometry on the jet flow and the acoustic field. Flow Turbul. Combust. (2016). doi:10.1007/s10494-016-9764-z
4. Cetin, M.O., Pauz, V., Meinke, M., Schröder, W.: Computational analysis of nozzle geometry variations for subsonic turbulent jets. Comput. Fluids **136**, 467–484 (2015)
5. Cetin, M.O., Pogorelov, A., Lintermann, A., Cheng, H.J., Meinke, M., Schröder, W.: Large-scale simulations of a non-generic helicopter engine nozzle and a ducted axial fan. In: High Performance Computing in Science and Engineering´ 15, pp. 389–405. Springer, Cham (2016)
6. Ewert, R., Schröder, W.: Acoustic perturbation equations based on flow decomposition via source filtering. J. Comput. Phys. **188**(2), 365–398 (2003)
7. Ewert, R., Schröder, W.: On the simulation of trailing edge noise with a hybrid LES/APE method. J. Sound Vibr. **270**(3), 509–524 (2004)
8. Freund, J.B.: Proposed inflow/outflow boundary condition for direct computation of aerodynamic sound. AIAA J. **35**(4), 740–742 (1997)
9. Geiser, G., Koh, S.R., Schröder, W.: Analysis of acoustic source terms of a coaxial helium/air jet. AIAA Paper 2011–2793 (2011)
10. Hartmann, D., Meinke, M., Schröder, W.: An adaptive multilevel multigrid formulation for Cartesian hierarchical grid methods. Comput. Fluids **37**(9), 1103–1125 (2008)
11. Hu, F.Q., Hussaini, M.Y., Manthey, J.L.: Low-dissipation and low-dispersion Runge-Kutta schemes for computational acoustics. J. Comput. Phys. **124**(1), 177–191 (1996)
12. Jeong, J., Hussain, F.: On the identification of a vortex. J. Fluid Mech. **285**, 69–94 (1995)
13. Johansson, S.: High order finite difference operators with the summation by parts property based on DRP schemes. Technical report, 2004–036 (2004)
14. Johnson, A.D., Xiong, J., Rostamimonjezi, S., Liu, F., Papamoschou, D.: Aerodynamic and acoustic optimization for fan flow deflection. AIAA paper, 2011–1156 (2011)
15. Koh, S.R., Geiser, G., Schröder, W.: Reformulation of acoustic entropy source terms. AIAA paper, 2011–2927 (2011)
16. Konopka, M., Meinke, M., Schröder, W.: Large-eddy simulation of shock-cooling-film interaction. AIAA J. **50**, 2102–2114 (2012)
17. Kunnen, R.P.J., Siewert, C., Meinke, M., Schröder, W., Beheng, K.D.: Numerically determined geometric collision kernels in spatially evolving isotropic turbulence relevant for droplets in clouds. Atmos. Res. **127**, 8–21 (2013)
18. Lintermann, A., Schlimpert, S., Grimmen, J.H., Günther, C., Meinke, M., Schröder, W.: Massively parallel grid generation on HPC systems. Comput. Methods Appl. Mech. Eng. **277**, 131–153 (2014)
19. Meinke, M., Schröder, W., Krause, E., Rister, T.: A comparison of second- and sixth-order methods for large-eddy simulation. Comput. Fluids **31**(4–7), 695–718 (2002)
20. Papamoschou, D., Shupe, R.S.: Effect of nozzle geometry on jet noise reduction using fan flow deflectors. AIAA paper 2006–2707 (2006)

21. Pardowitz, B., Tapken, U., Knobloch, K., Bake, F., Bouty, E., Davis, I., Bennett, G.: Core noise – identification of broadband noise sources of a turbo-shaft engine. AIAA paper 2014–3321 (2014)
22. Pogorelov, A., Meinke, M., Schröder, W.: Cut-cell method based large-eddy simulation of tip-leakage flow. Phys. Fluids **27**(7), 075106 (2015)
23. Pogorelov, A., Meinke, M., Schröder, W.: Effects of tip-gap width on the flow field in an axial fan. Int. J. Heat Fluid Flow (2016). doi:10.1016/j.ijheatfluidflow.2016.06.009
24. Pogorelov, A., Meinke, M., Schröder, W., Kessler, R.: Cut-cell method based large-eddy simulation of a tip-leakage vortex of an axial fan. AIAA paper 2015-1979 (2015)
25. Schneiders, L., Hartmann, D., Meinke, M., Schröder, W.: An accurate moving boundary formulation in cut-cell methods. J. Comput. Phys. **235**, 786–809 (2013)
26. Schröder, W., Ewert, R.: LES-CAA coupling. In: Large-Eddy Simulations for Acoustics. Cambridge University Press (2005)
27. Zhu, T., Carolus, T.H.: Experimental and numerical investigation of the tip clearance noise of an axial fan. GT2013-94100 (2014)